An experimental and numerical study of multi-pulse picosecond laser ablation on 316L Stainless Steel

TONG ZHOU,[1,2,*] YUCHAO HONG,[1] ZHENG FANG,[2] WALTER PERRIE,[2] YANG FEI,[2] YOUYOU HU,[1,*] STUART EDWARDSON,[2] GEOFF DEARDEN,[2]

[1] *School of Science, Jiangsu University of Science and Technology, Zhenjiang, 212100, China*
[2] *Laser Group, School of Engineering, University of Liverpool, Brownlow Street, Liverpool, L69 3GQ, UK*
* *tongzhou6@just.edu.cn & yyhu@just.edu.cn*

Abstract: An experimental and numerical study on 10 ps laser ablation of 316L stainless steel up to 400 hundred pulse exposure has been carried out. In this simulation, the material removal threshold temperature has been carefully discussed depending on the different ablation driving mechanisms. The influence of the instantaneous material removal has also been considered which will affect the calculation of the next pulse's absorption. For single-pulse ablation, the simulated ablation threshold F_{sim}=0.26 J/cm^2 is close to the fitted experimental result F_{0th}=(0.29 ± 0.01) J/cm^2. For multi-pulse ablation, the simulated ablation rate R_{sim}=11.4 nm/pulse is close to the fitted experimental result R_{exp}=(12.4±0.1) nm/pulse under 0.9 J/cm^2 fluence, while the simulated ablation rate R_{sim}=19.8 nm/pulse is slightly larger than the fitted experimental result R_{exp}=(16.1 ± 0.7) nm/pulse at 2.7 J/cm^2, providing good agreement between theory and experiment for both single and multi-pulse ablation. This study could be used to predict the multi-pulse laser processing performance, especially with the help of a machine learning method to find the best parameters automatically.

1. Introduction

Ultrafast laser whose pulse duration τ < 10 ps has been widely used in areas such as micro cutting [1], surface texturing [2], thin-film processing [3] due to the nature of ultrafast laser-material interactions with minimal heat conduction [4]. During the ultrafast laser ablation, the conduction electrons, excited by the single photon absorption, experience a dramatic increase of electron temperature T_e during the pulse. Then, the electron energy transfers to the lattice through the electron-phonon interaction, leading to a nonequilibrium temperature stage [4, 5] which is widely accepted by using the two-temperature model (TTM) [6] to evaluate.

During the past decade, a range of studies on ultrafast laser materials interaction, both theoretical and experimental have been carried out. For example, Metzner et al. [7] and Kumar et al. [8] studied the single pulse ablation on bulk metal by using TTM to predict the ablation depth and radius of single ultrashort pulse laser ablation of 316L stainless steel and Ti6Al4V alloy respectively. The ablation on dielectric materials like fused silica can also be simulated by the TTM [9, 10], as well as the thin-film ablation. For example, Thorstensen and Foss [11] analyze the variation of ablation thresholds when a silicon wafer is under different initial temperatures. Li et al. [12], and Olbrich et al. [13] predicted the ablation depth and radius on different thickness aluminium films, and a 'gentle' and 'strong' ablation crater were found when the film thickness is above 100 nm. Multi-layer thin film ablation can also be carried out. Zhou et al. [14] investigated the laser ablation on gold/glass film which was achieved by setting the electron insulation of electrons and thermal conduction in the glass layer as there are very few free electrons in dielectric materials. As a result, the two-temperature model is a powerful tool for studying the physics during ultrafast laser ablation on both bulk and thin films.

However, most of the studies on ultrafast TTM research are based on single-pulse ablation. For example, Leng et al. [15] integrated the single pulse laser energy and so equivalent to a multi-pulse for the numerical study. Zhang et al. [16] simulated the multi-pulse ablation on aluminium by assuming that the material removal rate is independent of pulse number due to the relatively low laser frequency (1 kHz). More recently, Kumar et al. [17] considered the material instantaneous removal rate during the simulation, experimentally and numerically investigating the 1-15 pulses high fluence femtosecond percussion drilling on Ti6Al4V alloy. Nevertheless, the accuracy of simulations remains challenging as the materials removal mechanisms and surface morphology changes during ablation will dramatically influence the accuracy of the simulation.

Moreover, the 'gentle' and 'strong' ablation [13, 18] will occur when 'low' and 'high' laser fluence is applied during the ablation. For example, spallation, occurring for the laser fluence slightly above the ablation threshold at 'low' fluence, will induce a high compressive pressure region under the laser irradiation area [19]. This induced high pressure will lead to the fracture of multiple nanometer layers and surface expansion in the skin depth which will finally separate the liquid layer [20, 21]. For high laser fluence, the phase explosion [22, 23] at the material's thermodynamic critical temperature is more dominant which will result the target into liquid and vapour droplets [24-26]. Hence the materials removal threshold temperature T_s should be carefully selected according to the applied laser parameters. In the meantime, the temperature governs thermo-dynamic parameters such as latent heat of evaporation, coupling factor, thermal conductivity and developing surface profile which should also be considered to get a more precise numerical prediction.

In this work, an experimental and numerical study on multi-pulse, 10 ps laser ablation of a polished 316L stainless steel is presented. The instantaneous material removal rate, surface morphology changes and the ablation threshold temperature were carefully considered to obtain more precise results yielding good agreement with experimental measurements. This 2D numerical computation for up to 400 hundred pulse exposure, closer to real-world application, can be further implemented into the machining learning process [27]. In this case, the desired results can be automatically chosen and transferred into the next calculation loop, which can save trial time and reduce manufacturing costs in the industry.

2. Methods

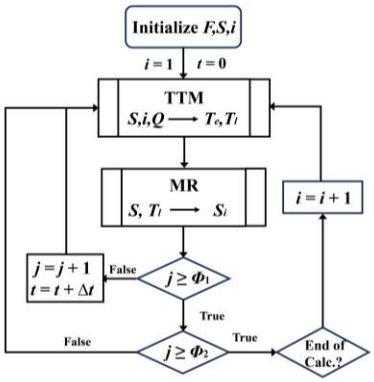

Parameter	Definition
F	Laser Fluence
S	Surface morphology
i	Number of the pulse
t	Time (pulse begin at t = 0 s)
Q	Input heat source
T_e	Electron temperature
T_l	Lattice Temperature
j	Number of the time loop
Φ_1	Steps for each pulse calculation
Φ_2	Total time steps
Δt	Time interval

Subroutine	Definition
TTM	Two-temperature model
MR	Material Removal

Subroutine name
Input(s) ⟶ *Output(s)*

Fig. 1. The flowchart of the ablation simulation of 10 ps laser on 316L stainless steel

The experiment was carried out on a Nd:YVO_4 seeded regenerative amplifier (High-Q IC-355-800 ps) laser which gives 5 kHz, 1064 nm, 10 ps linear polarized output beam. The beam energy was controlled by an attenuator system which is made by a halfwave plate and Glan laser polarizer. The beam was expanded through a diffraction limited telescope (M ~ ×3) and guided to the input aperture of a galvo system (Nutfield XLR8-10) via a periscope and focused by a

flat-field f-theta lens (f=100 mm) on the sample which was supported on x,y,z stages (Aerotech). The pulse number was controlled by a fast-mechanical shutter (Thorlabs SH05) and the pulse energy was calibrated under the galvo using a power meter (Coherent, LM-3). The focal spot size radius ($1/e^2$) is r_0=(11.1±0.1 μm), and the input beam diameter (before the galvo system input aperture) D_{in} is around 8 mm. More experimental details can be found in [3]. Each experimental data was measured 5 times and a Nikon DS-U2 microscope system coupled with the microscope NIS-Element D software and a WYKO NT1100 white light interferometer microscope was used to measure the 2D and 3D profiles of the ablated craters.

The numerical model proposed in this research combined TTM and material removal calculations, achieving by Coefficient from PDE and Deformed Geometry module respectively. The flowchart of the ablation simulation of 10 ps laser on 316L stainless steel is shown in Fig. 1. When the first pulse (i=1) with laser fluence F irradiates on the initial flat surface S, the amount of energy Q is absorbed in the material. Then, the electron temperature T_e and lattice temperature T_l will be calculated individually which is detailed in Section 3.1. Once the lattice temperature is high enough, the material removal stage will occur which is achieved by the Deformed Geometry function described in the Sec 3.2. The calculation of the i-th pulse's ablation will be finished when the number of the time loop j is large or equal to the steps for each pulse calculation Φ_1, and the i+1-th pulse calculation will start with the new surface morphology S_i. If not, the calculation will continue with a time interval Δt. The whole loop will be finished until the calculated time step j is large or equal to the total time step Φ_2.

3. Numerical Modelling

3.1 Two temperature model

For 10 ps laser ablation in this work, the two-temperature model (TTM) [6] is used to predict the temporal and spatial distribution of the electron and lattice temperatures throughout the ablation. For a 2D axisymmetric case, the physical model is governed by the equations:

$$C_e \frac{\partial T_e}{\partial t} = \nabla \cdot (k_e \nabla T_e) - G(T_e - T_l) + S(r,z,t) \tag{1}$$

$$C_l \frac{\partial T_l}{\partial t} = \nabla \cdot (k_l \nabla T_l) + G(T_e - T_l) \tag{2}$$

$$\nabla = \left[\frac{\partial}{\partial r}, \frac{\partial}{\partial z} \right] \tag{3}$$

where r is the distance from the laser spot centre and z is the penetration depth from the substrate surface. C_e/C_l and k_e/k_l represent the heat capacity and thermal conductivity of electron and lattice while T_e and T_l are the temperatures of electron and lattice, respectively. G is the electron-lattice coupling coefficient, and $Q(r, z, t)$ represents the absorbed laser heating source which can be described as [28]:

$$Q(r,z,t) = (1-R)\frac{F}{t_p} \exp\left(-2\frac{r^2}{r_0^2}\right) \cdot \exp\left(-4\ln 2 \frac{(t-t_0)^2}{(t_p)^2}\right) \exp(-\alpha z) \tag{4}$$

in which F is laser fluence, R is material reflectivity, t_p is temporal pulse length, r_0 is the $1/e^2$ radius of the laser beam, t_0 is the time when pulse peak arrives and α is the absorption coefficient of 316 Stainless Steel.

The numerical change of the phase state is considered by combining the latent heat of fusion H_M and vaporization H_V in the volumetric heat capacity of the lattice [13],

$$C_l = \rho \cdot \left[C_{l0} + \frac{H_M}{\Delta T \cdot \sqrt{2\pi}} \cdot e^{-\frac{1}{2}\cdot\left(\frac{T_l - T_M}{\Delta T}\right)^2} + \frac{H_V}{\Delta T \cdot \sqrt{2\pi}} \cdot e^{-\frac{1}{2}\cdot\left(\frac{T_l - T_V}{\Delta T}\right)^2} \right] \quad (5)$$

where C_{l0} represents the heat capacity constant of the material, and $\Delta T = 50$ K is used, which determines the width of the zone of phase change. T_M and T_V are the melting and vaporization temperatures, respectively.

The volumetric heat capacity of the electron C_e, coupling factor G and electron thermal conductivity k_e can be approximated as [7, 29]:

$$C_e = \left[2.677\times10^6 \exp(8.937\times10^{-6}\frac{T_e}{K}) + 2.987\times10^6 \exp(3.787\times10^{-4}\frac{T_e}{K}) \right] JK^{-1}m^{-3} \quad (6)$$

$$G = [2.837\times10^{18} \exp\left(-\left(\frac{\frac{T_e}{K} - 3007}{1.166\times10^4}\right)^2\right) + 2.993\times10^{18} \exp\left(-\left(\frac{\frac{T_e}{K} - 2.998\times10^4}{8.147\times10^4}\right)^2\right)] WK^{-1}m^{-3} \quad (7)$$

$$k_e = \left[\left(0.535\times\frac{10^4 T_e}{K} - 0.004 \right)\times10^3 \right] WK^{-1}m^{-1} \quad (8)$$

The reflectance of stainless steel depends on the irradiation laser wavelength, electron temperature and the optical properties of Fe, Cr and Ni [30]. By weighting the percentage of major elements of 316L (Fe70Cr17Ni13), the reflectance R can be given by [7]:

$$R = \left[11\exp\left(-\frac{0.00013T_e}{K}\right) + 59.2 \right] \% \quad (9)$$

Note that the reflectivity R was calculated up to an electron temperature of 25×10^3 K [29, 30]. The material parameters for solving TTM are given in Table 1. For the case that no data are available for stainless steel, the data for iron is used instead.

3.2 Axisymmetric model building

In order to save the computation time, a 2D axisymmetric finite element model was built through COMSOL 5.2. The computation domain was set as 40 μm × 10 μm with 80 ×100 elements in r and z direction respectively, and both directional element ratio was set to 5, as shown in Fig. 2. Zero flux boundary conditions were set on the right and bottom surface of the computation domain. The symmetric axis was adopted to the Gaussian distribution center of the input laser, and the laser source was irradiated at the top surface of the domain for the first pulse ablation. However, the changeable domain surface will influence the start surface of the Beer-Lambert law. In this case, a modification of the Beer-Lambert law in Eq. (4) has changed into,

$$Q(r,z,t) = (1-R)\frac{F}{t_p}\exp\left(-2\frac{r^2}{r_0^2}\right)\cdot\exp\left(-4\ln 2\frac{(t-t_0)^2}{(t_p)^2}\right)\exp\left(-\alpha\cdot\mathrm{abs}(z - D_{S_i}(r))\right) \quad (10)$$

where abs(z-$D_{Si}(r)$) means the absolute value of the expression, S_i is the i-th pulse surface morphology and $D_{Si}(r)$ means the ablated depth D at a distance r on the radial direction of the domain of the S_i.

The depth of the focus $Z_F = \frac{2.56M^2\lambda f^2}{D_{in}^2} \approx 1\ mm$, which is much larger than the μm scale in ablation depth of this work so that the spot size and incident laser intensity distribution were considered constant during the multi pulse ablation simulation. The deformed geometry module

was used to simulate the instant material removal during the processing. Prescribed Normal Mesh Velocity was added at the material top surface to estimate the deformation velocity of grid, v_{deform} , which can be determined by the energy balance at the top surface as [31]:

$$v_{deform} = \mathbf{V}_{deform} \cdot \mathbf{n} = \frac{\mathrm{F}_{\mathrm{vap}}}{\rho \cdot H_v} \tag{11}$$

in which case $\mathbf{V}_{deform}$ is the velocity of the matter leaving the interface, **n** means the normal vector of surface, and H_v is the latent heat of evaporation, and the thermal boundary condition F_{vap} can be governed by the ablative heat flux condition which is defined as:

$$\mathrm{F}_{\mathrm{vap}} = h(T) \cdot (T - T_s) \tag{12}$$

where T_s is the threshold temperature, and *h(T)* is a temperature-dependent heat transfer coefficient, while *h(T)*=0 for $T<T_s$ and increases linearly as $T>T_s$. The *h(T)* is a slope function with a steep slope, enforcing that the temperature of the solid cannot markedly exceed the ablation temperature. Note that both evaporation temperature T_v [32] and the phase explosion at the materials thermodynamic critical temperature (T_c) [24, 25] were used as threshold value T_s depending on incident fluence.

Table 1. Laser parameters and thermo-physical properties of 316L Stainless Steel [33-36]

	Parameter	Value
Laser parameters	Laser fluence **F** [J/cm^2]	0.9, 1.8,2.7…
	Wavelength **λ** [nm]	1064
	Radius $\mathbf{w_0}$ [μm]	11.1
	Pulse duration $\mathbf{t_p}$ [ps]	10
Thermo-physical parameters of 316L Stainless Steel	Coefficient of electron heat capacity $\mathbf{k_0}$ [J m^{-3} K^{-1}]	134.5
	Absorption coefficient **α** [m^{-1}]	5.3e7
	Specific heat capacity $\mathbf{C_{l0}}$ [J kg $^{-1}$ K^{-1}]	450
	Thermal conductivity of lattice $\mathbf{k_l}$ [W m^{-1} K^{-1}]	23
	Critical Temperature $\mathbf{T_c}$ [K]	9324
	Fermi Temperature $\mathbf{T_f}$ [K]	1.28e5
	Electron-lattice coupling at room temperature $\mathbf{g_0}$ [W m^{-3} K^{-1}]	2.45e17
	Melting temperature $\mathbf{T_m}$ [K]	1881
	Evaporation temperature, $\mathbf{T_v}$ [K]	3300
	Latent heat of fusion, $\mathbf{H_M}$ [kJ/kg]	2.47e5
	Evaporation enthalpy, $\mathbf{H_V}$ [kJ/kg]	6.36e6
	Density, $\boldsymbol{\rho_{Al}}$ [kg m^{-3}]	7950

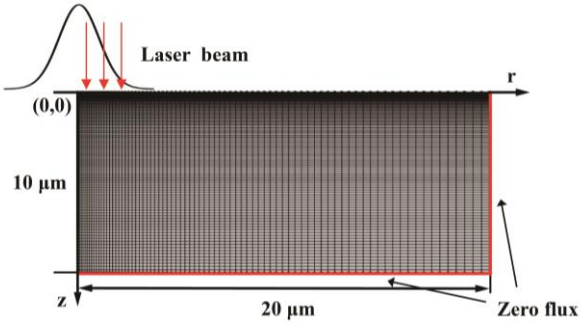

Fig. 2. The geometric model of 316 L stainless steel and boundary conditions

4. Results and discussion

4.1 Experimental results

The ablation threshold on stainless steel was measured using the following equations [37],

$$D^2 = 2r_0^{\,2}\ln\left(\frac{F_0}{F_{th}}\right) \tag{13}$$

$$F_0 = \frac{2E_p}{\pi r_0^{\,2}} \tag{14}$$

where D is the measured ablated crater diameter, r_0 is the laser spot radius, F_{th} is the ablation threshold, F_0 is the peak fluence and E_p is the pulse energy. Both single-pulse ablation and multi-pulse ablation were measured, and the pulse energy was set as E_p=4 μJ, 6 μJ, …, 22 μJ. For multi-pulse ablation calculation, the ablated radius D was measured with the pulse energy E_p=2.0 μJ, 4.0 μJ, …, 20.0 μJ and pulse number N = 1, 100, 200 and 400 pulses, respectively.

A plot of D^2 versus E_p is shown in Fig. 3(a), each data point was measured 5 times and error bars represent 1σ. The single pulse ablation threshold was fitted according to the model as $F_{th0(1)}$ = (0.29 ± 0.01) J/cm^2, which is close to Jaeggi et al. [38] result whose F_{th0}=0.31 J/cm^2 and Zhao et al. [40] result whose F_{th0}=0.28 J/cm^2 under the 10ps, 1064nm laser's irradiation. Similarly, the ablation thresholds of multi-pulse ablation were fitted as $F_{th0}(100)$=(0.16 ± 0.01) J/cm^2, $F_{th0}(200)$=(0.14 ± 0.01) J/cm^2 and $F_{th0}(400)$=(0.12 ± 0.01) J/cm^2.

The incubation model describes the relationship between the single-pulse ablation threshold $F_{th0}(1)$ and the multi-pulse ablation threshold $F_{th}(N)$ in form [39]

$$F_{th}(N) = F_{th}(1)\cdot N^{S-1} \tag{15}$$

where S is the incubation coefficient and is measured as S=(0.85 ± 0.01), shown in Fig 3(b). The typical values of S in the range between 0.8 and 0.9 were found with this method in the case of multi-shot laser ablation of metals at relatively low repetition rates (< 100 kHz) [40-42] and close to the value, S=0.858 measured by Zhao et al. [39].

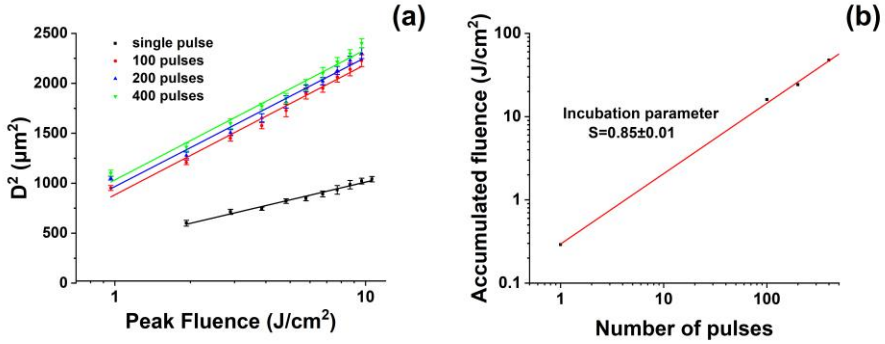

Fig. 3. The ablation threshold measurements of 10 ps 1064 nm laser on 316L Stainless steel (a) Graph of squared ablation diameter D^2 versus E_p for the single, 100, 200 and 400 pulse ablation (b) The incubation coefficient factor for 10 ps,1064 nm, 5 kHz ablation on 316L Stainless Steel

The optical images and cross section profiles of multi-pulse ablation at fluence F=0.9 J/cm^2 and 2.7 J/cm^2 are shown in Fig 4. The spherically symmetric dark areas surrounding the ablation pits is due to the backward flux re-deposition during the multi-pulse ablation [43]. The ablated depth increases with pulse number, and a linear relationship could be found in both cases. The ablation depths were measured to be as follows: D_{ab}=(0.91 ± 0.10) μm, (2.16 ± 0.13) μm, (4.61 ± 0.16) μm for laser fluence F = 0.9 J/cm^2, and for laser fluence F=2.7 J/cm^2, D_{ab}=(1.64 ± 0.09) μm, (3.39 ± 0.12) μm, (6.27 ± 0.29) μm at 100, 200 and 400 pulses respectively.

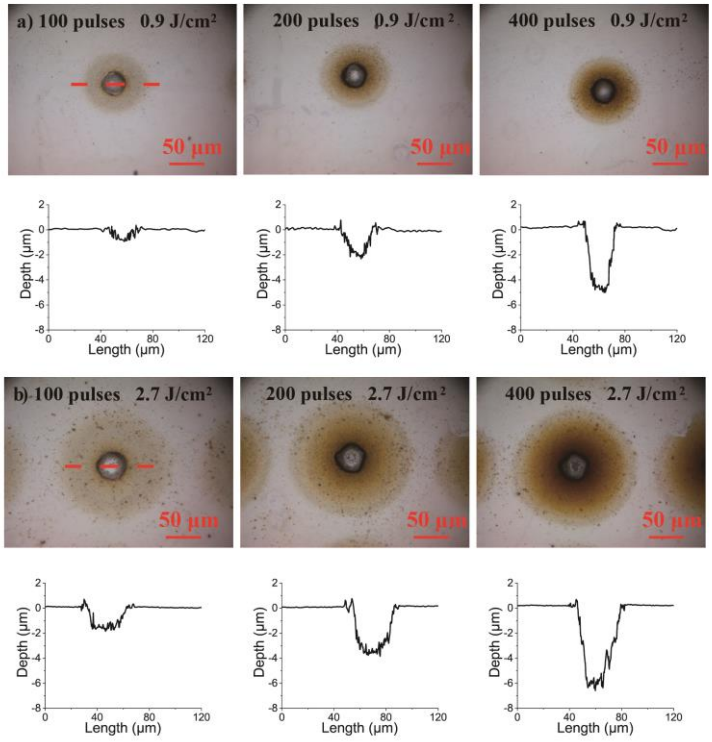

Fig. 4. The optical images and cross section profile of 10 ps laser ablation on 316L Stainless Steel at 100, 200 and 400 pulses. (a) F=0.9 J/cm^2 (b) 2.7 J/cm^2

4.2 Numerical results

In this work, a range of laser fluence were used. Due to the different driving mechanisms (spallation and phase explosion) at 'low' and 'high' laser fluence, the threshold temperature T_s in Eq. (12) should be carefully considered. The threshold temperature T_s was first set as the material's thermodynamic critical temperature T_c for all fluence, $T_s = T_c$, and the electron and lattice temperature along with a time scale of 100 ps at center point (0,0) in Fig. 1 was calculated and shown in Fig. 5(a).The corresponding calculated maximum electron temperature T_e = 11,300 K, 15,200 K, 18,900 K while the lattice temperature takes 10.3 ps, 7.2 ps, 6.1 ps to reach the critical temperature of the stainless steel at fluence F = 0.9, 1.8 and 2.7 J/cm^2, respectively. When laser fluence F=0.9 J/cm^2, the maximum T_e=11300 K which is close to the T_s=9324 K. There will be only a small amount of the material reaches the T_c while the rest of the materials remain the solid or liquid state. In this case, it may not be physically reasonable to use T_c as threshold temperature for material removal. Moreover, at 'low' fluence regime, the spallation is predominated, and the materials are removed mainly by the laser-induced pressure [20, 21]. When 'high' laser fluence $F \geq 0.9$ J/cm^2 is applied, the maximum T_e is much larger than the critical temperature T_c and the lattice temperature T_l indicates a mixture of liquid and gas material whose phenomena is predominated by the phase explosion. In this case, the threshold temperature T_s is set as the evaporation temperature, T_s=T_V=3300K while the laser fluence $F <$ 0.9, and T_s=T_c=9324 K when laser fluence $F \geq 0.9$ J/cm^2. In addition, a logarithmic form of temperature-time dependence in a second periodic (100 ps – 10 µs) when the laser fluence F=2.7 J/cm^2 is also shown in Fig. 5(a). It could be seen that the lattice and electron temperature both reached the room temperature at 7.27 µs whereas the inter-pulse period is 0.2 ms in this work. Therefore, the possible heat accumulation in the multi-pulse ablation has not been considered in this simulation.

The lattice and electron temperature at 'low' laser fluence near the ablation threshold are calculated to test this assumption, and the fluence where the lattice temperature just reaches the evaporation temperature T_v is considered as the ablation threshold for 316L stainless steel. Fig. 5(b) shows the electron and lattice temperature with an inset yellow region, enlarged. The lattice temperature just rises above the evaporation temperature (T_v = 3300 K) at the laser fluence F=0.26 J/cm^2, which is close to the experimental measurement $F_{th0}(1)$=(0.29 ± 0.01) J/cm^2, whereas the ablation threshold when critical temperature T_c is used is calculated as F_{sim} =0.61 J/cm^2 (not shown). This simulation result supports our assumption that at 'low' laser fluence, the ablation threshold temperature should be chosen as evaporation temperature T_v instead of the critical temperature (T_c) which is relevant at 'high' laser fluence. To verify the quantity of the used transport coefficient with the TTM, a comparison of the electron and lattice temperature along 100 ps with our and Wang et al. [44] work are shown in Fig. 5(c). It could be seen that our work has a good fit with Wang et al.'s work. The slight difference might contribute to the constant reflectivity R = 0.51 in Wang et al.'s work.

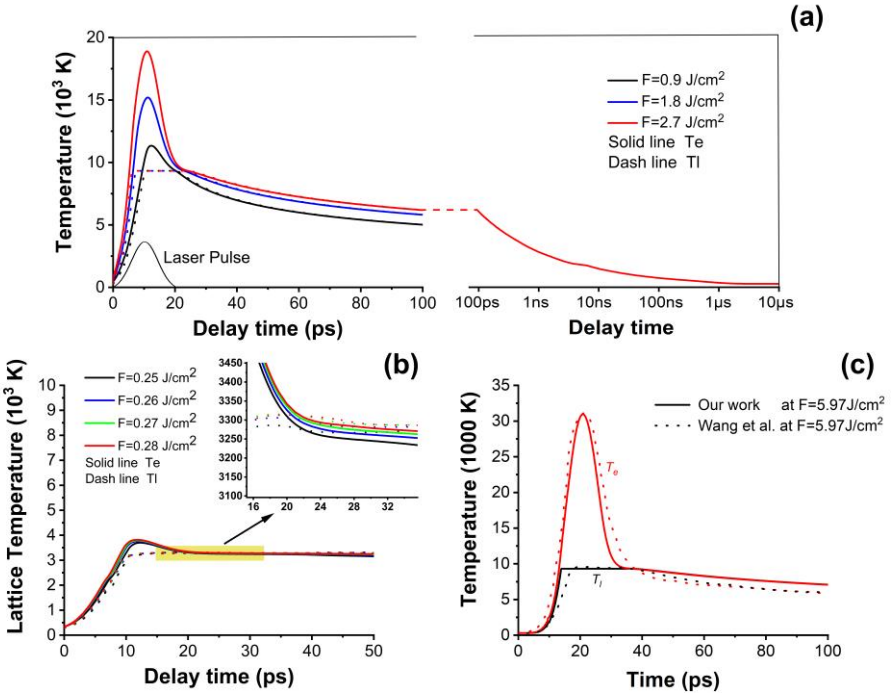

Fig. 5. The electron and lattice temperature at laser spot center (0,0). (a) laser fluence F = 0.9, 1.8 and 2.7 J/cm^2. (b) laser fluence F = 0.25, 0.26, 0.27 and 0.28 J/cm^2, and ablation threshold is recognized at 0.26 J/cm^2 due to the lattice temperature at this fluence first reaching the evaporation temperature of the 316L Stainless Steel (T_v = 3300 K). (c) A validation of the quantity of the used transport coefficient with the TTM.

The distribution of 2D lattice temperature at 'high' laser fluence F=2.7 J/cm^2 under multi-pulse ablation is shown in Fig. 6. At 5 ps delay after the first pulse ablation, the maximum surface temperature raised to ~ 6500 K, but there is no material removal since the surface temperature is below the critical temperature, T_c. Then the temperature continues to rise until T_c at 7.5 ps delay when phase explosion and material removal occurs. An obvious surface depression can be observed at 25 ps, which is deeper and wider at 50 ps delay, and further evaporation after 50 ps delay is negligible. In this case, the recessional surface profile of the i-th pulse at 100 ps is exported as a txt. file and inserted in the i+1-th pulse ablation's calculation, as shown in Eq. (10). In this case, a more accurate material removal region can be simulated. Hence, an iterative calculation can be carried out for higher pulse numbers.

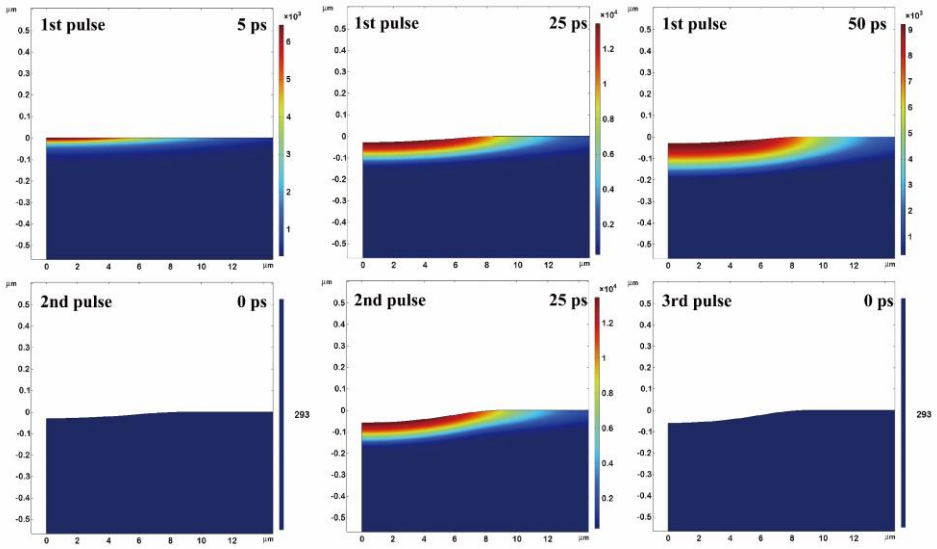

Fig. 6. The temporal distribution of 2D lattice temperature and developing surface profile at laser fluence F = 2.7 J/cm^2 under 1st, 2nd and 3rd pulse ps ablation.

The developing surface recession at laser fluence F = 2.7 J/cm^2 under 1st, 50th, 100th, 200th, 300th and 400th pulses at 50 ps is shown in Fig. 7. After the first pulse irradiation, a 0.021 μm deep and 8.77 μm radius crater has been formed. Then, the depth increased to 1.03 μm, 2.04 μm, 4.03 μm, 6.02 μm, 7.97 μm while the ablation radii increased to 9.33 μm, 10.04 μm, 10.49 μm, 10.74 μm, 11.01 μm after 50, 100, 200, 300 and 400 pulse exposure, respectively. In particular, the ablation rate almost follows a linear increase, but the increments of the ablated radius are decreasing which illustrates the incubation effect of multi-pulse ablation.

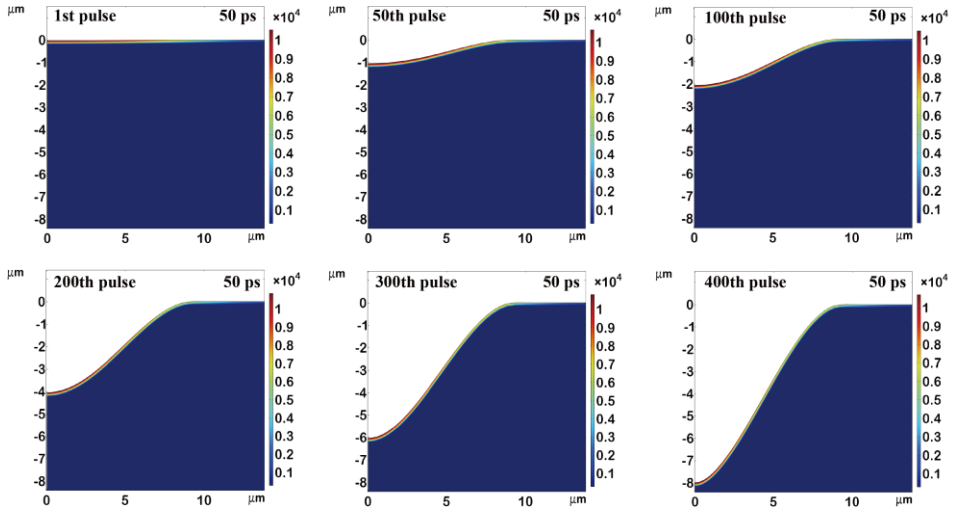

Fig. 7. The surface temperature and recession at laser fluence F = 2.7 J/cm^2 under 1st, 50th, 100th, 200th, 300th and 400th pulses at 50 ps.

The experiential and numerical ablated rate of 10 ps (1064nm) laser on 316L stainless steel is also compared and shown in Fig. 8. For 'low' fluence F=0.9 J/cm^2, the simulated ablated rate $R_{sti\text{-}l}$=11.4 nm/pulse is close the calculated experimental result $R_{exp\text{-}l}$=(12.4±0.1) nm/pulse. The simulated and experimental ablated depth at 100, 200, 300 and 400 pulses are $D_{sim\text{-}l}$=1.15 μm, 2.28 μm, 3.40 μm, 4.52 μm and $D_{exp\text{-}l}$=(0.91±0.10) μm, (2.16±0.13) μm, (3.72±0.14) μm,

(4.61±0.16) μm, respectively. It could be seen that the simulated results were first larger than the experimental results, then it became lower than the experimental results after 350 pulses ablation, with good agreement. This change might result in the increased laser absorption due to the increased effect of surface roughness which is only necessary when the pulse number is high at low laser fluence [45].

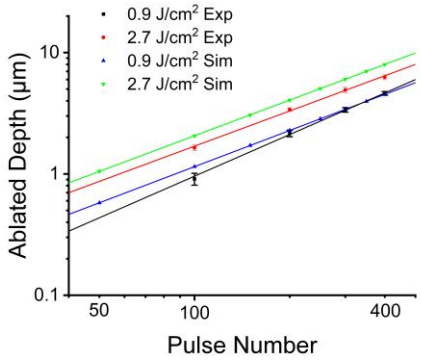

Fig. 8. Log10-log10 figure of pulse number versus simulated and experimental results of ablation depth under 0.9 J/cm^2 and 2.7 J/cm^2 fluence at 10 ps (1064nm @5kHz) laser ablation on 316L Stainless Steel.

However, the simulated results at 'high' fluence F=2.7 J/cm^2, $R_{sti\text{-}h}$=19.8 nm/pulse, are ~ 20% higher than the calculated experimental result $R_{exp\text{-}h}$=(16.1 ± 0.7) nm/pulse, and the simulated and experimental ablated depth at 100, 200, 300 and 400 pulses exposure are $D_{sim\text{-}h}$=2.06 μm, 4.05 μm, 6.04 μm, 7.99 μm and $D_{exp\text{-}h}$ =(1.64±0.09) μm, (3.39±0.12) μm, (4.92 ±0.25) μm, (6.27±0.29) μm, respectively. This difference might be caused by the inaccuracy in calculated reflectivity around and above an electron temperature of 25,000 K [30], while reflectivity reduces with the increasing pulse number and surface roughness [46]. The backward flux re-deposition [43] might also reduce the effective ablation rate/pulse, especially at 'high' fluence, as 'thicker' oxidization layer needs to be removed for multi-pulse ablation[47]. In our previous study on stainless steel with incident fluence F=9.0 J/cm^2 and 10 ps pulse length, the plasma lifetime (1/e) was measured as (9.2 ±1.0) ns, yielding an electron temperature T_e ~ 7500 K after 40 ns delay [43]. The possible plasma shielding might also influence the final absorption during the laser ablation which might cause errors in the calculation results.

Other physics (for example, spallation, phase transition, stress confinement and density-dependent collision frequency) which has not been considered in this model, will also bring the errors into the results. For 316L stainless steel under 10 ps pulse duration, the heating time τ_{heat} is defined by the pulse duration which is longer than the mechanical expansion time, $\tau_{heat} \approx \tau > \tau_{mech}$, as the 316L stainless steel's typical electron-photon interaction time τ_{ep} is around 1-3 ps [29] and the mechanical expansion time τ_{mech} is around 5 ps [48]. In this case, the low heat conduction and high electron-phonon coupling will confine the laser energy near the surface, contributing to the laser-induced stress relaxation and the thermoelastic stress which is large enough to cause the photomechanical spallation [49]. This photothermal phase explosion can cause around a 25 % drop in energy specific ablation volume (ESAV) which is the ratio of the removal volume V_{abl} and the irradiated pulse energy $E_{p,}$ compared with the ESAV at 0.9 J/cm^2 and 2.7 J/cm^2 under 10 ps pulse duration [48]. Hence, the ablation efficiency will decrease as the increment of the laser fluence. As our model has not considered the influence of the spallation and phase explosion, it could bring a relatively large error at 'high' fluence.

Moreover, the phase transition during the ablation will influence the material's optical properties which are related to the varying electron collision frequencies. The electron-electron collision frequency υ_{ee} is often proportional to the electron temperature $\upsilon_{ee} \propto T_e^{\,2}$ and the

electron-ion collision frequency is directly proportional to the lattice temperature $\upsilon_{ei} \propto T_l$ [50]. In this case, the density changes of the 316L stainless steel within lattice temperature, density decrease, and solid-liquid phase transition, all influencing optics via varying collision frequencies which will bring additional differences between the simulation and experiment. It was found that there is a nearly constant upward shift of the effective electron frequency υ_{eff} along with the increase of the electron temperature, and an abrupt increase of the υ_{eff} will occur when the solid material transfer into liquid. reflecting the major decrease of thermal conductivity [51]. This density-dependent collision and plasma frequency will dramatically affect the real part of material dielectric function $\Delta\varepsilon_r$ [51] and further influence the total absorption through the ablation. In this case, without considering the density dependence in this model will bring larger errors at high laser fluence, as there is a more obvious density change at high fluence ablation [47]. As a result, without considering the ultrafast laser ablation efficiency by stress confinement [52] and the material's optical properties change due to the density transition [51] will bring the errors in this simulation, and higher errors could be found at 2.7 J/cm^2 whose absorption has been more impacted as previous discussion.

5. Conclusions

This method yields encouraging results although representing an approximate picture of the complex ablation process as the single and multiple pulse ablation exposure has been studied experimentally and numerically. The material removal module was used to simulate the instantaneous material removal, which can obtain a more accurate result. Material removal mechanisms such as spallation and phase explosion under different laser fluences have been carefully considered. The threshold temperature T_s was set as evaporation temperature $T_s = T_v = 3300$ K for fluence F < 0.9 J/cm^2, and the critical temperature $T_s = T_c = 9324$ K for fluence F ≥ 0.9 Jcm^{-2} according to the different ablation driving mechanisms under the 'low' and 'high' laser fluence. In this case, an excellent agreement between experiment and simulation could be achieved as the predicted single pulse ablation threshold F_{sim}=0.26 J/cm^2 is close to the experimental measurement $F_{0th}(1)$=(0.29±0.01) J/cm^2. The resulting recession surface parameters were used in an iterative procedure to increase the accuracy of the total absorption after multi-pulse exposure. and 1 to 400 pulses ablation were performed with instant material removal at different temporal scales. By using this method, the predicted ablation rate for multi-pulse ablation, $R_{sti\text{-}l}$ = 11.4 nm/pulse is close to the experimental result $R_{sti\text{-}l}$=(12.4 ± 0.1) nm/pulse at 0.9 J/cm^2, while at higher laser fluence F = 2.7 J/cm^2, the simulated and calculated experimental ablated rate are $R_{sti\text{-}h}$=19.8 nm/pulse and $R_{exp\text{-}h}$=(16.1 ± 0.7) nm/pulse, respectively. This method is a very versatile tool optimized for variable materials: it works across different industrial applications, for example, thin-film processing, laser-induced periodic spatial structure formation, laser drilling, which can save the trial and error costs in manufacturing. Furthermore, this model can be implemented into the machining learning process [27], which can directly choose the desired results and transfer them into the next calculation.

Funding. Jiangsu Provincial Key Research and Development Program (BE2022143); Wenzhou Major Scientific and Technological Innovation Project (ZG2022008).

Disclosures. The authors declare no conflicts of interest.

Data availability. Data underlying the results presented in this paper are not publicly available at this time but may be obtained from the authors upon reasonable request.

References

1. K. L. Wlodarczyk, A. Brunton, P. Rumsby, and D. P. Hand, "Picosecond laser cutting and drilling of thin flex glass," Opt. Laser Eng. **78**, 64-74 (2016).
2. Z. Fang, T. Zhou, W. Perrie, M. Bilton, J. Schille, U. Löschner, S. Edwardson, and G. Dearden, "Pulse Burst Generation and Diffraction with Spatial Light Modulators for Dynamic Ultrafast Laser Materials Processing," Mater. **15**, 9059 (2022).

3. T. Zhou, Z. Fang, W. Perrie, Y. Fei, S. Edwardson, and G. Dearden, "Experimental and numerical modelling of picosecond laser ablation of thin aluminium Polyethylene Terephthalate (PET) films," Opt. Laser Technol. **151**, 107976 (2022).
4. K. C. Phillips, H. H. Gandhi, E. Mazur, and S. Sundaram, "Ultrafast laser processing of materials: a review," Adv. Opt. Photonics **7**, 684-712 (2015).
5. B. Mueller, and B. Rethfeld, "Nonequilibrium electron–phonon coupling after ultrashort laser excitation of gold," Appl. Surf. Sci. **302**, 24-28 (2014).
6. S. Anisimov, B. Kapeliovich, and T. Perelman, "Electron emission from metal surfaces exposed to ultrashort laser pulses," Zh. Eksp. Teor. Fiz **66**, 375-377 (1974).
7. D. Metzner, M. Olbrich, P. Lickschat, A. Horn, and S. Weißmantel, "Experimental and theoretical determination of the effective penetration depth of ultrafast laser radiation in stainless steel," Lasers in Manufacturing and Materials Processing **7**, 478-495 (2020).
8. K. K. Kumar, G. Samuel, and M. Shunmugam, "Theoretical and experimental investigations of ultra-short pulse laser interaction on Ti6Al4V alloy," J. Mater. Process. Tech. **263**, 266-275 (2019).
9. B. Chimier, O. Utéza, N. Sanner, M. Sentis, T. Itina, P. Lassonde, F. Légaré, F. Vidal, and J.-C. Kieffer, "Damage and ablation thresholds of fused-silica in femtosecond regime," Phys. Rev. B **84**, 094104 (2011).
10. P. Pan, H. Song, Z. Yang, G. Ren, J. Xiao, X. Chen, and J. Xu, "Thermal field modeling and experimental analysis in laser-assisted machining of fused silica," Silicon **13**, 3163-3176 (2021).
11. J. Thorstensen, and S. Erik Foss, "Temperature dependent ablation threshold in silicon using ultrashort laser pulses," J. Appl. Phy. **112** (2012).
12. Q. Li, H. Lao, J. Lin, Y. Chen, and X. Chen, "Study of femtosecond ablation on aluminum film with 3D two-temperature model and experimental verifications," Appl. Phys. A **105**, 125-129 (2011).
13. M. Olbrich, E. Punzel, R. Roesch, R. Oettking, B. Muhsin, H. Hoppe, and A. Horn, "Case study on the ultrafast laser ablation of thin aluminum films: dependence on laser parameters and film thickness," Appl. Phys. A **122**, 215 (2016).
14. S. Zhou, K. Zhao, and H. Shen, "Ablation of gold film on different substrates by ultrafast laser," Opt. Laser Technol. **132**, 106495 (2020).
15. B. Leng, E. Tang, H. Luo, C. Huang, Y. Han, C. Chen, M. Chang, K. Guo, and L. He, "Research on thermal and mechanical effects of Al/PTFE reactive materials irradiated by femtosecond pulsed laser," Infrared Phys. Techn. **119**, 103961 (2021).
16. J. Zhang, Y. Chen, M. Hu, and X. Chen, "An improved three-dimensional two-temperature model for multi-pulse femtosecond laser ablation of aluminum," J. Appl. Phy. **117** (2015).
17. K. Kiran Kumar, G. Samuel, and M. Shunmugam, "An in-depth investigation into high fluence femtosecond laser percussion drilling of titanium alloy," Proceedings of the Institution of Mechanical Engineers, Part B: Journal of Engineering Manufacture **237**, 601-617 (2023).
18. X. Wang, Y. Huang, C. Li, and B. Xu, "Numerical simulation and experimental study on picosecond laser ablation of stainless steel," Opt. Laser Technol. **127**, 106150 (2020).
19. E. Leveugle, D. S. Ivanov, and L. V. Zhigilei, "Photomechanical spallation of molecular and metal targets: molecular dynamics study," Appl. Phys. A **79**, 1643-1655 (2004).
20. H. Tamura, T. Kohama, K. Kondo, and M. Yoshida, "Femtosecond-laser-induced spallation in aluminum," J. Appl. Phys. **89**, 3520-3522 (2001).
21. C. Wu, M. S. Christensen, J.-M. Savolainen, P. Balling, and L. V. Zhigilei, "Generation of subsurface voids and a nanocrystalline surface layer in femtosecond laser irradiation of a single-crystal Ag target," Phys. Rev. B **91**, 035413 (2015).
22. C. Phipps, *Laser ablation and its applications* (Springer, 2007).
23. E. G. Gamaly, "The physics of ultra-short laser interaction with solids at non-relativistic intensities," Phys. Reports **508**, 91-243 (2011).
24. D. A. Willis, and X. Xu, "Heat transfer and phase change during picosecond laser ablation of nickel," Int. J. Heat Mass Tran. **45**, 3911-3918 (2002).
25. S. Wang, Y. Ren, C.-W. Cheng, J. Chen, and D. Tzou, "Micromachining of copper by femtosecond laser pulses," Appl. Surf. Sci. **265**, 302-308 (2013).
26. B. Wu, and Y. C. Shin, "A simple model for high fluence ultra-short pulsed laser metal ablation," Appl. Surf. Sci. **253**, 4079-4084 (2007).
27. S. Chugh, S. Ghosh, A. Gulistan, and B. Rahman, "Machine learning regression approach to the nanophotonic waveguide analyses," J. Lightwave Technol. **37**, 6080-6089 (2019).
28. X. Wang, C. Ma, C. Li, M. Kang, and K. Ehmann, "Influence of pulse energy on machining characteristics in laser induced plasma micro-machining," J. Mater. Process. Tech. **262**, 85-94 (2018).
29. E. Bévillon, J.-P. Colombier, B. Dutta, and R. Stoian, "Ab initio nonequilibrium thermodynamic and transport properties of ultrafast laser irradiated 316L stainless steel," J. Phys. Chemistry C **119**, 11438-11446 (2015).
30. E. Bévillon, R. Stoian, and J.-P. Colombier, "Nonequilibrium optical properties of transition metals upon ultrafast electron heating," J. Phys.: Condens. Matter **30**, 385401 (2018).
31. L. Ben-Mahfoud, E. Silaeva, R. Stoian, and J.-P. Colombier, "Structural instability of transition metals upon ultrafast laser irradiation," Phys. Rev. B **104**, 104104 (2021).

32. L. Chen, Z. Chen, K. Shimada, M. Mizutani, and T. Kuriyagawa, "Electric field analysis coupled with the two-temperature model to elucidate the generation process of laser-induced periodic surface structure," J. Mater. Process. Tech. **305**, 117601 (2022).
33. C. A. Dold, *Picosecond laser processing of diamond cutting edges* (ETH Zurich, 2013).
34. J. J. Valencia, and P. Quested, "Thermophysical properties," Modeling for casting and solidification processing **189** (2001).
35. B. J. Simonds, J. Sowards, J. Hadler, E. Pfeif, B. Wilthan, J. Tanner, C. Harris, P. Williams, and J. Lehman, "Time-resolved absorptance and melt pool dynamics during intense laser irradiation of a metal," Phys. Rev. Appl. **10**, 044061 (2018).
36. M. Palengat, G. Chagnon, D. Favier, H. Louche, C. Linardon, and C. Plaideau, "Cold drawing of 316l stainless steel thin-walled tubes: experiments and finite element analysis," Int. J. Heat Mass Tran. **70**, 69-78 (2013).
37. J. Liu, "Simple technique for measurements of pulsed Gaussian-beam spot sizes," Opt. Lett. **7**, 196-198 (1982).
38. B. Jaeggi, B. Neuenschwander, M. Schmid, M. Muralt, J. Zuercher, and U. Hunziker, "Influence of the pulse duration in the ps-regime on the ablation efficiency of metals," Phys. Procedia **12**, 164-171 (2011).
39. W. Zhao, W. Wang, G. Jiang, B. Q. Li, and X. Mei, "Ablation and morphological evolution of micro-holes in stainless steel with picosecond laser pulses," Int. J. Adv. Manuf. Tech. **80**, 1713-1720 (2015).
40. G. Raciukaitis, M. Brikas, P. Gecys, and M. Gedvilas, "Accumulation effects in laser ablation of metals with high-repetition-rate lasers," in High-Power Laser Ablation VII(Spie2008), pp. 725-735.
41. P. Mannion, J. Magee, E. Coyne, G. O'connor, and T. Glynn, "The effect of damage accumulation behaviour on ablation thresholds and damage morphology in ultrafast laser micro-machining of common metals in air," Appl. Surf. Sci. **233**, 275-287 (2004).
42. F. Di Niso, C. Gaudiuso, T. Sibillano, F. Mezzapesa, A. Ancona, and P. Lugarà, "Influence of the repetition rate and pulse duration on the incubation effect in multiple-shots ultrafast laser ablation of steel," Phys. Procedia **41**, 698-707 (2013).
43. T. Zhou, S. Kraft, W. Perrie, J. Schille, U. Löschner, S. Edwardson, and G. Dearden, "Backward flux re-deposition patterns during multi-spot laser ablation of stainless steel with picosecond and femtosecond pulses in air," Mater. **14**, 2243 (2021).
44. X. Wang, Y. Huang, C. Li, and B. Xu, "Numerical simulation and experimental study on picosecond laserablation of stainless steel" Opt. Laser Technol 127106150 (2020).
45. H. Mustafa, M. Mezera, D. T. A. Matthews, and G. Römer, "Effect of surface roughness on the ultrashort pulsed laser ablation fluence threshold of zinc and steel," Appl. Surf. Sci. **488**, 10-21 (2019).
46. C. McDaniel, A. Flanagan, and G. M. O'Connor, "Evidence for increased incubation parameter in multi-pulse ablation of a Pt: SS alloy using a femtosecond laser at high repetition rates," Appl. Surf. Sci. **295**, 1-7 (2014).
47. J. Winter, S. Rapp, M. Spellauge, C. Eulenkamp, M. Schmidt, and H. P. Huber, "Ultrafast pump-probe ellipsometry and microscopy reveal the surface dynamics of femtosecond laser ablation of aluminium and stainless steel," Appl. Surf. Sci. **511**, 145514 (2020).
48. J. Winter, M. Spellauge, J. Hermann, C. Eulenkamp, H. P. Huber, and M. Schmidt, "Ultrashort single-pulse laser ablation of stainless steel, aluminium, copper and its dependence on the pulse duration," Opt. Express **29**, 14561-14581 (2021).
49. L. V. Zhigilei, Z. Lin, and D. S. Ivanov, "Atomistic modeling of short pulse laser ablation of metals: connections between melting, spallation, and phase explosion," J. Phys. Chem. C **113**, 11892-11906 (2009).
50. P. M. Chaikin, T. C. Lubensky, and T. A. Witten, *Principles of condensed matter physics* (Cambridge university press Cambridge, 1995).
51. J. Winter, D. Redka, J. Minár, M. Schmidt, and H. P. Huber, "Resolving transient temperature and density during ultrafast laser ablation of aluminum," Appl. Phys. A **129**, 665 (2023).
52. D. Redka, J. Winter, C. Gadelmeier, A. Djuranovic, U. Glatzel, J. Minár, and H. P. Huber, "Control of ultrafast laser ablation efficiency by stress confinement due to strong electron localization in high-entropy alloys," Appl. Surf. Sci. **594**, 153427 (2022).